Available online at www.sciencedirect.com
ScienceDirect
Journal of Molecular Catalysis A: Chemical 262 (2007) 216–226
JOURNAL OF MOLECULAR CATALYSIS A: CHEMICAL
www.elsevier.com/locate/molcata

Scanning tunneling microscopy (STM) and tunneling spectroscopy (TS) studies of polyoxometalates (POMs) of the Wells–Dawson structural class

In Kyu Song [a], Mahmoud S. Kaba [b], Kenji Nomiya [c], Richard G. Finke [d], Mark A. Barteau [b,*]

[a] *School of Chemical and Biological Engineering, Seoul National University, Shinlim-dong, Kwanak-ku, Seoul 151-744, Republic of Korea*
[b] *Department of Chemical Engineering, University of Delaware, Newark, DE 19716, USA*
[c] *Department of Materials Science, Kanagawa University, Hiratsuka, Kanagawa 259-1293, Japan*
[d] *Department of Chemistry, Colorado State University, Ft. Collins, CO 80523, USA*

Available online 22 August 2006

Abstract

Presented in this work is an extensive scanning tunneling microscopy (STM) study of self-assembled monolayers of polyoxometalates (POMs) belonging to the Wells–Dawson structural class. The effects of cation and framework atom substitutions in these POMs and their salts have been examined. The Wells–Dawson POMs and their salts formed self-assembled and well-ordered arrays on graphite surfaces. Tunneling spectroscopy (TS) measurements revealed that these POMs exhibited negative differential resistance (NDR) behavior in their tunneling spectra. The arrays of vanadium-substituted POMs, $H_{6+x}[P_2Mo_{18-x}V_xO_{62}]$ ($x = 1, 2, 3$), showed periodicities of ca. 11 Å × 14 Å. The shapes and periodicities of the corrugations in the STM images are consistent with the structure and the characteristic dimensions of the Wells–Dawson polyanion, $[P_2Mo_{18}O_{62}]^{6-}$, as determined from X-ray crystallography studies. Moreover, the STM results indicated that framework substitutions and increases in the number of charge-compensating protons had negligible effects on the array periodicities. Various salts of trisubstituted Wells–Dawson POMs, $Q[P_2W_{15}Nb_3O_{62}]$ ($Q = Na_9$, Cs_9, $(Bu_4N)_9$, $(Bu_4N)_5Na_3(Re(CO)_3)$), also formed two-dimensional monolayer arrays with various periodicities. For this class of POM salts, the periodicities were greater than the anion dimensions, reflecting the size of the counter cation (Q). TS measurements revealed the positions of the counter cations in the POM salt arrays, and the positions were consistent with the cation positions found in the bulk crystal structures. For each class of Wells–Dawson anions, it was shown that the packing of the polyanions in the monolayers was not identical to, but resembled that found in bulk cleavage planes of the corresponding POM. A correlation between NDR peak voltage and reduction potential established for both POM series revealed that more reducible POMs showed NDR peaks at less negative applied voltage. In other words, a less negative NDR peak voltage corresponded to a higher reduction potential. This trend is consistent with those previously elucidated for POM catalysts with the Keggin structure.

Keywords: Scanning tunneling microscopy; Tunneling spectroscopy; Wells–Dawson polyoxometalate (POM); Negative differential resistance (NDR); Reduction potential

1. Introduction

Polyoxometalates (POMs), also known as heteropolyacids (HPAs), are early transition-metal oxide anion clusters that have found numerous successful applications in homogeneous and heterogeneous catalysis [1–4]. They are multifunctional catalysts with tunable redox and acid–base properties. These properties can be altered by replacing protons in the POM with alkali metals or vice versa, or by substituting one or more of the framework transition-metal atoms with a different metal [1–4]. Among the different structural classes of these materials, the Keggin-type anions [5] ($[XM_{12}O_{40}]^{q-}$, where X = P, Si, Ge, etc., and M = Mo, W, V, etc.) constitute the largest group on which extensive research has been done. POMs belonging to the Wells–Dawson structural class [6] ($[X_2M_{18}O_{62}]^{q-}$, where X = P, Si, Ge, etc., and M = Mo, W, V, etc.) have also garnered significant interest as catalysts, especially in the synthesis of methyl *tert*-butyl ether (MTBE) [7,8]. For this reaction, Wells–Dawson-type POMs were found to be more active per acid equivalent than Keggin-type POMs or other conventional acid catalysts such as H_2SO_4 and H-ZSM-5 in both homogeneous [7] and heterogeneous [8] systems. Wells–Dawson-type POMs have also been

* Corresponding author. Tel.: +1 302 831 8905; fax: +1 302 831 8201.
E-mail address: barteau@udel.edu (M.A. Barteau).

1381-1169/$ – see front matter © 2006 Elsevier B.V. All rights reserved.
doi:10.1016/j.molcata.2006.08.028

used as components of a microporous solid resembling a zeolite, with the hope that the transition-metal atoms in the anion would serve as active sites for shape-selective oxidation reactions in well-defined micropores [9]. Additionally, they have been used in the pillaring of Mg_3Al layered double hydroxides (LDHs) [10]. Unlike the Keggin-type anion, α-$[H_2W_{12}O_{40}]^{6-}$, which has a nearly spherical (T_d) symmetry and thus limits the possible gallery heights upon intercalation in the LDH galleries, the lower D_{3h} (cylindrical) symmetry of the Wells–Dawson tungstophosphate anion, α-$[P_2W_{18}O_{62}]^{6-}$, can lead to gallery micropores of different sizes, depending on its interlayer orientation [10].

Similar to approaches undertaken to fine-tune catalytic properties of Keggin-type POMs, it has also been desirable to modify Wells–Dawson-type POMs for specific applications. Hence, mono (iron(III))-substituted Wells–Dawson-type tungstophosphates have been synthesized [11] and their catalytic activities for olefin epoxidation, aliphatic and aromatic hydrocarbon hydroxylation [12], and for H_2O_2 and NO_2 reduction [13] have been examined. Trisubstituted heteropolytungstates, $[P_2W_{15}Nb_3O_{62}]^{9-}$, have also been synthesized in order to covalently attach catalytically active organometallic groups [14–17]. For example, it has been shown that $(Bu_4N)_5Na_3$(1,5-COD)Ir$[P_2W_{15}Nb_3O_{62}]$ can serve as a precursor to a novel $[P_2W_{15}Nb_3O_{62}]^{9-}$ polyoxoanion-stabilized nanocluster catalyst active for olefin hydrogenation reactions [18]. POMs have also been used as surface modifiers in order to develop specific anion-substrate recognition in catalysis and biological applications, and to regulate membrane permeability for potential chemotherapy [1]. The understanding of surface structures and properties of POMs is crucial for these applications.

Scanning tunneling microscopy (STM) has been used to examine surfaces of bulk crystals [19,20] and of self-assembled monolayers [21–38] of Keggin-type POMs deposited on highly oriented pyrolytic graphite (HOPG) surfaces. These comprehensive STM studies showed that substitution of protons by alkali metals in Keggin-type HPAs results in increased lattice constants of the ordered POM arrays, while substitution of the framework transition-metal atoms had no significant impact on these spacings [23–38]. Tunneling spectroscopy (TS) measurements on the discrete Keggin anions observed in the STM images revealed distinctive current peaks in the current–voltage (*I–V*) spectra; this behavior is referred to as negative differential resistance (NDR) [21,23–38]. The voltages at which NDR occurred have been correlated with the reduction potentials of the Keggin-type POM catalysts [25,26,29,30,32,34–38].

Members of other structural classes were previously imaged with molecular resolution by STM [27]; they included members from the Wells–Dawson [6] ($H_7[P_2Mo_{17}VO_{62}]$), the Droege–Finke [39] ($Na_{16}[Cu_4(P_2W_{15}O_{56})_2]$), and the Pope–Jeannin–Preyssler [40] ($K_{12.5}Na_{1.5}[NaP_5W_{30}O_{110}]$) classes. In this report, we present a detailed STM study of self-assembled monolayers of several members of the Wells–Dawson structural class, $Na_6[P_2Mo_{18}O_{62}]$, $H_{6+x}[P_2Mo_{18-x}V_xO_{62}]$ ($x = 1, 2, 3$), and four kinds of cation substituted-$[P_2W_{15}Nb_3O_{62}]$. The effects of cation and framework atom substitutions on the ordered arrays of Wells–Dawson polyanions were examined. Their molecular shapes and two-dimensional surface arrays obtained by STM were compared to simulated images obtained using molecular simulation software. The current–voltage (*I–V*) behavior of each sample was also probed by TS measurements. The NDR peak voltages were then correlated with the reduction potentials of Wells–Dawson POM catalysts.

2. Experimental

2.1. Sample preparation and deposition

$H_{6+x}[P_2Mo_{18-x}V_xO_{62}]\cdot nH_2O$ ($x = 1, 2, 3$) samples were supplied by Dr. George Coulston (DuPont Company, Wilmington, DE), and $Na_6[P_2Mo_{18}O_{62}]\cdot 24H_2O$ was provided by Prof. Craig L. Hill (Emory University, Atlanta, GA). $Na_9[P_2W_{15}Nb_3O_{62}]\cdot 23H_2O$, $Cs_9[P_2W_{15}Nb_3O_{62}]\cdot 8H_2O$, $(Bu_4N)_9[P_2W_{15}Nb_3O_{62}]$, and $(Bu_4N)_5Na_3(Re(CO)_3)[P_2W_{15}Nb_3O_{62}]$ were synthesized and characterized using procedures described elsewhere [14–17,41,42–46]. Approximately 0.01 M aqueous solutions of each sample were prepared. A drop of the sample solution was then deposited on a freshly cleaved highly oriented pyrolytic graphite (HOPG) surface and allowed to dry in air for approximately 1 h.

2.2. STM and TS measurements

STM images were acquired using a TopoMetrix TMX-2010 instrument in air. Mechanically formed $Pt_{0.9}Ir_{0.1}$ tips were used. STM images were acquired in the constant current mode at a tunneling current of 1–2 nA and a sample bias of 100 mV. Calibration procedures have been enumerated elsewhere [23–38]. The STM images were recorded with tips which first demonstrated both reproducible atomic resolution images of HOPG and two-dimensional fast Fourier transform (two-dimensional FFT) derived periodicities consistent with the standard value for graphite. No image presented in the present work was Fourier filtered, and the reported lattice constants are average values determined by performing two-dimensional FFT analyses on at least three STM images per sample, with each image acquired using a different tip at a different scan rate (40,000–80,000 Å/s). TS measurements were taken using both TopoMetrix TMX-2010 and LK Technologies LK 1000 instruments to confirm consistency and reproducibility. TS measurements were performed at least 10 times each using at least three different tips for each sample to obtain more accurate and reproducible results, and to provide a basis for statistical analyses. The STM probe was positioned above the POM molecule of interest for the TS measurements. The tunneling current was then monitored while the bias voltage was ramped from −2 V to +2 V. The voltage axis in the tunneling spectrum represents the potential applied to the sample relative to that of the tip. Cleavage planes of bulk crystals were generated from published X-ray diffraction (XRD) results using a Biosym Cerius II Molecular Simulations software on a Silicon Graphics workstation.

3. Results and discussion

3.1. STM and TS investigation of $[P_2Mo_{18-x}V_xO_{62}]^{(6+x)-}$ ($x = 0, 1, 2, 3$) series

The structure of the Wells–Dawson anion, α-$[P_2Mo_{18}O_{62}]^{6-}$, is shown in Fig. 1. The polyanion consists of two defect Keggin-type fragments, α-$[PMo_9O_{34}]^{9-}$ [47]. Each fragment consists of a central PO_4 tetrahedron sharing corners with nine MoO_6 octahedra—the octahedra are somewhat distorted from their ideal geometry. Three MoO_6 octahedra form a compact group by sharing edges, while the remaining six octahedra in each of the α-$[PMo_9O_{34}]^{9-}$ fragments form a zigzag ring by alternately sharing edges and corners. The two fragments are linked by six nearly linear Mo–O–Mo bonds. The resulting structure, α-$[P_2Mo_{18}O_{62}]^{6-}$, has approximate D_3 symmetry. The calculated minimum van der Waals diameters of the anion from published X-ray structure determinations [47] are 10.98 Å × 14.48 Å (width × height of the molecule in Fig. 1). $[P_2Mo_{18-x}V_xO_{62}]^{(6+x)-}$ ($x = 1, 2, 3$) anions are expected to have comparable dimensions, but XRD structure determinations of these have not been published.

Fig. 2 shows two typical STM images of $Na_6[P_2Mo_{18}O_{62}]$ and $H_9[P_2Mo_{15}V_3O_{62}]$ on graphite, along with their unit cells.

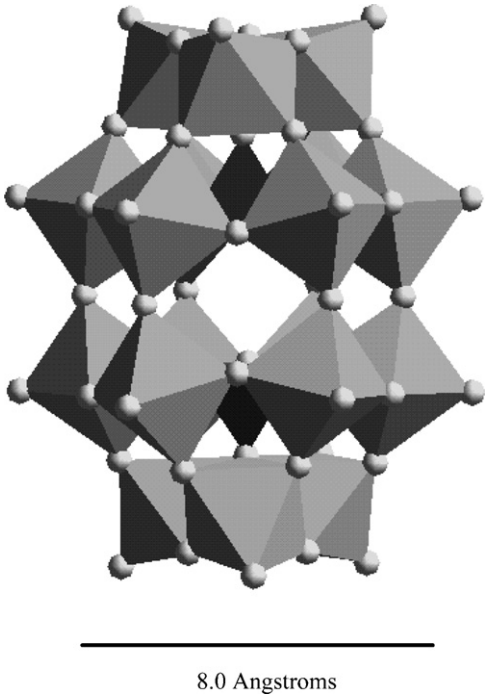

Fig. 1. Polyhedral representation of the molecular structure of the Wells–Dawson anion, α-$[P_2Mo_{18}O_{62}]^{6-}$.

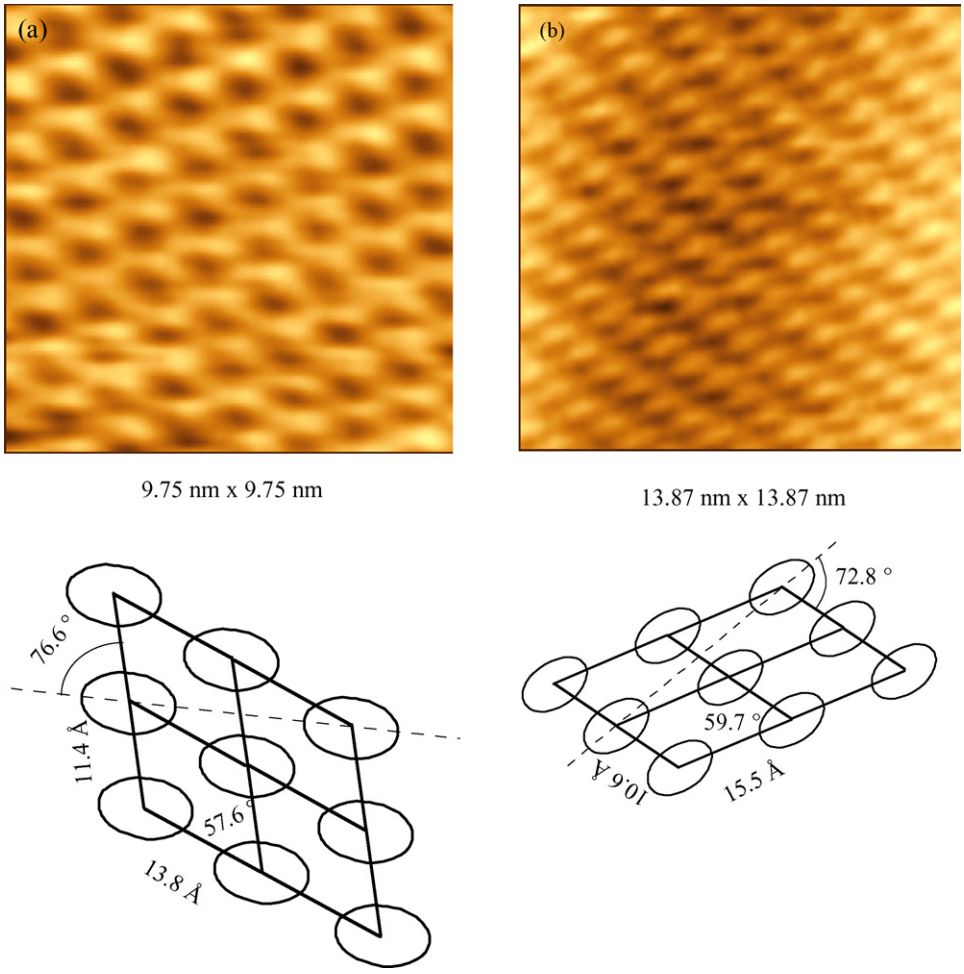

Fig. 2. STM images and unit cells of (a) $Na_6[P_2Mo_{18}O_{62}]$ and (b) $H_9[P_2Mo_{15}V_3O_{62}]$ arrays on HOPG.

Table 1
Lattice constants of arrays of Wells–Dawson POMs with the $[P_2Mo_{18-x}V_xO_{62}]^{(6+x)-}$ ($x = 0, 1, 2, 3$) framework

POM	Periodicity of array (Å × Å)	Included angle (°)	Unit cell area (Å^2)
$Na_6[P_2Mo_{18}O_{62}]$	11.4 × 13.8	57.6	132.8
$H_7[P_2Mo_{17}V_1O_{62}]$	10.3 × 13.1	71.6	128.0
$H_8[P_2Mo_{16}V_2O_{62}]$	11.9 × 14.4	54.3	139.2
$H_9[P_2Mo_{15}V_3O_{62}]$	10.6 × 15.5	59.7	141.9

The STM images presented in Fig. 2 were horizontally leveled but not Fourier filtered. These images clearly showed well-ordered two-dimensional arrays of Wells–Dawson polyanions. Self-assembled, well-ordered arrays were observed over the large scan areas, up to 0.1 μm × 0.1 μm (not shown here). The periodicities of the arrays of each sample are listed in Table 1. Both the shape and periodicities of the corrugations in the STM images are consistent with the dimensions of the prolate spheroidal Wells–Dawson structure as determined from XRD [47]. Further evidence that the corrugations observed in the images were derived from discrete Wells–Dawson anions and not from graphite or Moiré anomalies [48,49] was obtained from TS measurements. In the TS measurements, the STM tip was positioned above a corrugation (bright feature in the image), and the tunneling current was measured as the sample bias voltage was ramped from negative to positive sample bias.

A typical *I–V* spectrum taken at a bright feature in the STM image of $Na_6[P_2Mo_{18}O_{62}]$ in Fig. 2(a) is shown in Fig. 3(a). This spectrum shows a distinctive current peak referred to as negative differential resistance (NDR) at −0.90 V. The NDR peak voltage was defined as the voltage where the maximum current was observed in this region. The STM images in this work were obtained at positive sample biases with respect to the tip. This means that electrons flow from the tip to the sample in the imaging mode of operation. NDR behavior in the tunneling spectra of POMs is observed at negative sample biases, i.e., when electrons tunnel from the sample to the tip [25,26,28,30,34,35,38]. In fact, there is some variation in both NDR peak position and intensity between spectra even on single component arrays, most likely due to variations in positioning the tip precisely for each measurement. In order to obtain more reproducible results and to provide a basis for statistical analyses (the voltage resolution of *I–V* spectra was 0.05 V), the NDR measurements were carried out at least 10 times each using at least three different tips for each sample. Fig. 3(b) shows the distribution of NDR peak voltages of $Na_6[P_2Mo_{18}O_{62}]$ arrays. The NDR peak voltages exhibited a monomodal distribution with a statistical mean value of -0.93 ± 0.13 V. The peak in the fitted distribution at −0.93 V can be taken as the representative NDR peak voltage for this POM catalyst. The most reproducible NDR peak voltage of $Na_6[P_2Mo_{18}O_{62}]$ arrays was found to be −0.90 V, as in Fig. 3(a). The most reproducible NDR peak voltages and statistical mean values measured for Wells–Dawson POM salts with the $[P_2Mo_{18-x}V_xO_{62}]^{(6+x)-}$ ($x = 0, 1, 2, 3$) framework are summarized in Table 2. NDR has also been observed in the *I–V* spectra of polyoxoanions belonging to other structural classes [21,23–38],

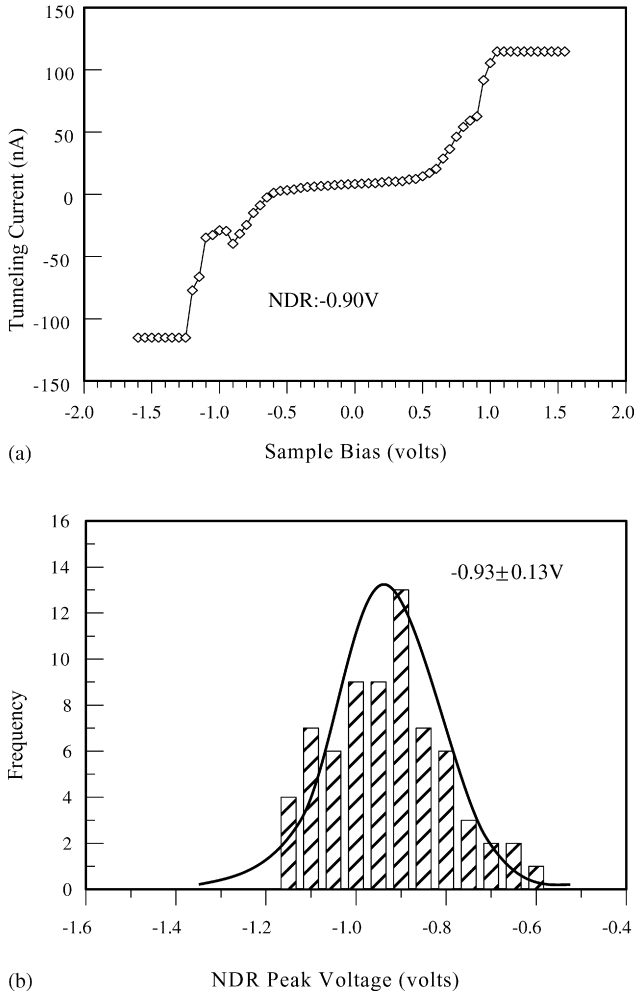

Fig. 3. (a) A typical *I–V* spectrum taken at $Na_6[P_2Mo_{18}O_{62}]$ corrugations (bright features) in Fig. 2(a) showing NDR behavior at −0.90 V. (b) Distribution of NDR peak voltages of $Na_6[P_2Mo_{18}O_{62}]$ arrays with a statistical mean value of -0.93 ± 0.13 V.

and thus its appearance provides evidence that the corrugations in the STM images of Fig. 2 indeed are Wells–Dawson anions. The characteristic NDR peak voltage of POMs can also serve as a fingerprint of POM identity, as demonstrated in previous reports investigating the mixed arrays of Keggin–Keggin [31] and Keggin–Wells–Dawson [33] POMs.

The Wells–Dawson anions in STM images are aligned in rows along their minor axes. Moreover, the principal molecular axes of the polyanions for the samples (Fig. 2) are aligned with

Table 2
Most reproducible NDR peak voltages and statistical mean values measured for Wells–Dawson POMs with the $[P_2Mo_{18-x}V_xO_{62}]^{(6+x)-}$ ($x = 0, 1, 2, 3$) framework

POM	Most reproducible NDR peak voltage (statistical mean value) (V)
$Na_6[P_2Mo_{18}O_{62}]$	−0.90 (-0.93 ± 0.13)
$H_7[P_2Mo_{17}V_1O_{62}]$	−0.65 (-0.65 ± 0.08)
$H_8[P_2Mo_{16}V_2O_{62}]$	−0.55 (-0.58 ± 0.07)
$H_9[P_2Mo_{15}V_3O_{62}]$	−0.80 (-0.83 ± 0.10)

respect to each other. The alignment can easily be seen from the unit cell schematics. All of the rows (the minor axes) are slightly staggered with respect to each other; hence, this type of packing (staggering) permits the anions to be more densely packed on the surface than if the anions were packed end-to-end along their major axes. A similar packing scheme is also found in the bulk crystal structure of $Na_6[P_2Mo_{18}O_{62}]$ [47]. In the $Na_6[P_2Mo_{18}O_{62}]\cdot 24H_2O$ crystals, there are three kinds of crystallographically different sodium ions, Na(1), Na(2), and Na(3). Each of them is always coordinated to two oxygen atoms in $[P_2Mo_{18}O_{62}]^{6-}$ anion. Na(1) and Na(2) are coordinated to two oxygen atoms in two different $[P_2Mo_{18}O_{62}]^{6-}$ anions, while Na(3) is coordinated to two oxygen atoms which belong to the same polyanion. The O–Na(1)–O bridges connect symmetry-related groups in the anions along the *z*-direction, thereby forming a zigzag chain (staggering) in this direction. These zigzag chains are then connected by O–Na(2)–O bridges in the *y*-direction, resulting in the formation of infinite layers that are parallel to the *yz*-plane of the crystal. Finally, the layers are held together by O–Na(3)–H_2O–Na(1)–O linkages (all of the water molecules associated with the crystal are coordinated to sodium ions).

Fig. 4 shows the (0 1 0) plane of $Na_6[P_2Mo_{18}O_{62}]\cdot 24H_2O$ at a depth of 0.50 of the unit cell, based on published XRD data [47]. The crystalline water molecules are omitted in this figure for simplicity, so that the positions of the sodium counter ions (dark, unattached spheres) can be easily discerned. The inter-anionic distance measured along the minor axis of the polyanions in this plane is 14.81 Å, while that measured along the major axis is 17.76 Å. These dimensions are greater than the measured periodicities of the polyanion arrays observed with the STM, listed in Table 1. It is evident that a major contributor to these differences is the water of crystallization which is present in the bulk

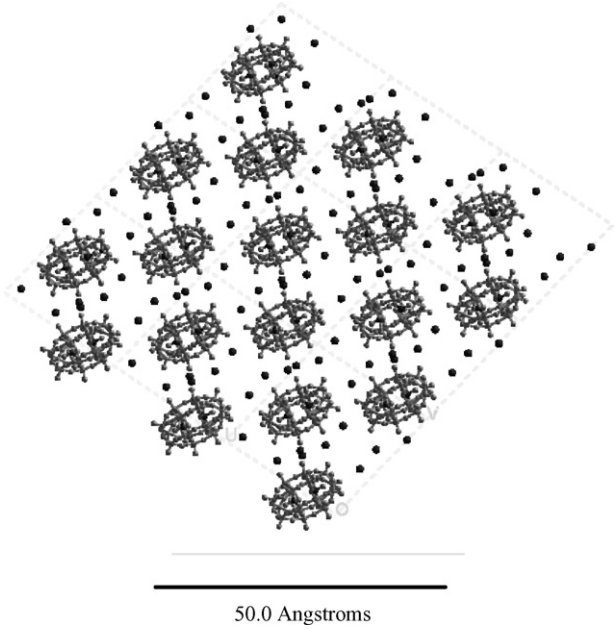

Fig. 4. The (0 1 0) plane of the bulk crystal of $Na_6[P_2Mo_{18}O_{62}]\cdot 24H_2O$: dark, unattached spheres represent Na cations, and water molecules have been omitted.

crystal, but is presumably minimal in the surface monolayers. In a previous study involving Keggin-type polyanions, it was demonstrated that the surface arrays of both $H_4PMo_{11}VO_{40}$ and $H_8PMo_{10}VCuO_{40}$ had almost identical lattice constants (10.6 Å and 10.7 Å, respectively) although the latter has twice as many charge-compensating protons as the former [23]. Since each proton is hydrated in the bulk crystal, one would expect that by doubling the number of protons (and therefore, the potential number of hydrated protons), the lattice of the monolayer would expand to accommodate the water molecules [23]. However, the STM results show that the number of charge-compensating protons and the water of crystallization in the bulk POM crystals had negligible effects on the lattices of the two-dimensional POM monolayers. This was also evidenced from the STM images obtained in air and in a humidity-free glove box, showing no difference in periodicities of two-dimensional arrays [23]. Therefore, the differences between the inter-anionic distances measured in the bulk crystal of $Na_6[P_2Mo_{18}O_{62}]\cdot 24H_2O$ and the periodicities of the two-dimensional arrays of $Na_6[P_2Mo_{18}O_{62}]$ are likely due to the lack of a significant number of water molecules in the $Na_6[P_2Mo_{18}O_{62}]$ monolayer. A comparison of the two structures shows that while the rows of polyanions in both structures are staggered with respect to each other, the staggering appears to be much more pronounced in the STM images (Fig. 2(a)) than in the bulk (Fig. 4). For the monolayer structures that are formed by polyanions on flat graphite surfaces, it has been shown that the packing motifs implied are inherently different from those found in the bulk crystals because of the absence of intermolecular interactions in the direction normal to the graphite surface [21,23–38]. Hence, the monolayers are not truncated planes of the bulk crystals, and one should not expect exact correspondence between them [27]. Although the exact number of water molecules in the two-dimensional monolayer arrays was not determined experimentally, it is believed that the lack of crystalline water molecules in the monolayers could also lead to the differences seen in the packing of the Wells–Dawson polyanions, as consistently observed in the Keggin-type POM monolayers [23].

The periodicities of the arrays of $H_{6+x}[P_2Mo_{18-x}V_xO_{62}]$ ($x = 1$, 2, and 3) do not show any particular trend, although they are all generally consistent with the dimensions of the Wells–Dawson anion. The slight differences in the periodicities of the Wells–Dawson anions of $H_7[P_2Mo_{17}V_1O_{62}]$ (13.1 Å) and those of $H_8[P_2Mo_{16}V_2O_{62}]$ and $H_9[P_2Mo_{15}V_3O_{62}]$ (14.4 Å and 15.5 Å, respectively) may be due to experimental errors, possibly arising from physical contacts between the STM tip and the adsorbed anions of the latter two POMs. Nevertheless, there is good agreement between the unit cell areas of the arrays. That the differences in periodicities are not due to the framework atom substitutions can be inferred from earlier work [23]. Song et al. showed that framework substitution in Keggin-type molybdophosphates, which subsequently led to different charges on the anions and to different numbers of protons required for charge compensation, had almost no effect on the two-dimensional structures or lattice spacing, even when the charge on the polyanion was doubled [23]. That work [23] was supported by results of XRD measurements [50] of the anion structure for single

crystals of $H_{2.6+x}Cu_{0.2}[PMo_{12-x}V_xO_{40}]$ ($x = 1, 2, 3$). Further STM studies on surface arrays of Keggin-type tungstomolybdophosphoric acids have shown that the spacings between the anions in these monolayers were also unaffected by framework substitutions [26,28,35]. Therefore, based on these results [23,26,28,35], the slight increases in the periodicities of the Wells–Dawson vanadomolybdophosphates ($H_8[P_2Mo_{16}V_2O_{62}]$ and $H_9[P_2Mo_{15}V_3O_{62}]$) are likely not due to framework substitutions in the molybdophosphates.

3.2. STM and TS investigation of $[P_2W_{15}Nb_3O_{62}]^{9-}$ series

Trisubstituted Wells–Dawson polyanions, B-$[P_2W_{15}Nb_3O_{62}]^{9-}$, were first synthesized in order to compare them to their Keggin-type counterparts, $[SiW_9Nb_3O_{40}]^{7-}$, and to determine their properties [14–17,42–46]. The trisubstituted Keggin-type polyanions were shown to contain sufficient surface oxygen charge density to covalently attach organic cations such as $CpTi^{3+}$ and $(C_5Me_5)Rh^{2+}$, and thus that work demonstrated the first Keggin anion-supported organometallic complexes [51–56]. In the trisubstituted Keggin anions, spectroscopy studies indicated that the organometallic moieties attach (regiospecifically) to only one of several types of surface oxygen sites with *C*s symmetry. In other words, the $CpTi^{3+}$ and $(C_5Me_5)Rh^{2+}$ groups preferentially attach to a B-type triad of edge-sharing MO_6 ($M = V^{5+}$, Nb^{5+}) octahedra [51–56]. Similar studies with B-$[P_2W_{15}Nb_3O_{62}]^{9-}$ also revealed that organometallic moieties can be supported at the C_{3v} symmetry site in the three adjacent, B-type, edge-sharing NbO_6 octahedra (triad) [14–17,42–46]. To probe their catalytic properties, several different tetraalkylammonium and other alkali salts, most notably $(Bu_4N)_5Na_3$(1,5-COD)Ir$[P_2W_{15}Nb_3O_{62}]$, were subsequently synthesized [14–18,42–46,57]. It has been shown that $(Bu_4N)_5Na_3$(1,5-COD)R$[P_2W_{15}Nb_3O_{62}]$ (R = Ir, Rh) is a catalyst precursor for olefin hydrogenation [18], and leads to a nanocluster catalyst with high stability and catalytic lifetime (190,000 total turnovers for R = Rh) [57].

Fig. 5 shows a polyhedral representation of $[P_2W_{15}Nb_3O_{62}]^{9-}$, as determined from XRD [41]. The anion is formed as a result of the base degradation of the Wells–Dawson α-$[P_2W_{18}O_{62}]^{6-}$ to α-$[P_2W_{15}O_{56}]^{12-}$ via the removal of one end cap. Therefore, it has the Wells–Dawson, α-$[P_2W_{18}O_{62}]^{6-}$ (D_{3h} symmetry) structure, but with the W atoms in one end cap of the three edge-sharing WO_6 octahedra replaced by three Nb atoms. The symmetry of the anion is close to C_{3v}. Fig. 6 shows STM images and unit cells of $[P_2W_{15}Nb_3O_{62}]^{9-}$ anions deposited as tetrabutylammonium and alkali salts. These STM images were horizontally leveled but not Fourier filtered. The images also showed well-ordered two-dimensional arrays of these polyanions on graphite surfaces with periodicities that are consistent with the anion structure and dimensions, plus those of the charge-compensating, counterion spacers. The self-assembled, well-ordered arrays were observed over scan areas up to 0.1 μm × 0.1 μm. Fig. 7 illustrates a large scan-area image for $(Bu_4N)_5Na_3(Re(CO)_3)[P_2W_{15}Nb_3O_{62}]$. Periodicities for each of the arrays in Fig. 6 are summarized in Table 3.

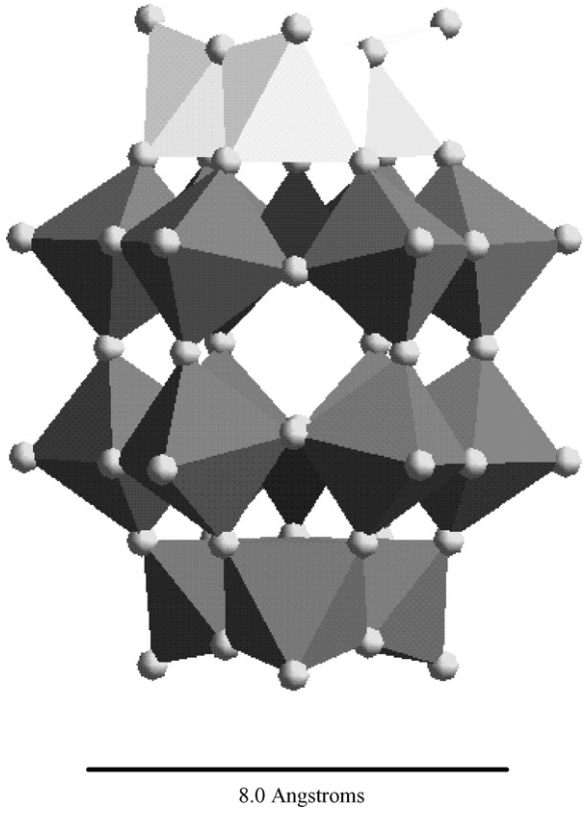

Fig. 5. Polyhedral representation of the molecular structure of the Wells–Dawson anion, B-$[P_2W_{15}Nb_3O_{62}]^{9-}$.

Note the much larger unit cell areas for samples with bulky counterions.

Previous studies with Keggin alkali molybdophosphates have shown that when protons of the POMs were replaced by alkali cations such as K^+ and Cs^+, the spacings between the Keggin anions in the two-dimensional monolayers on graphite increased correspondingly to accommodate the larger cations [23]. This observation is consistent with the secondary structure of bulk POMs, as proposed by Misono [58]. According to this model, POMs in the solid crystalline state are comprised of heteropolyanions (which are considered as the primary structure), cations (protons and/or metals), water of crystallization and/or organic molecules [58]. The secondary structure is very labile; polar molecules can be absorbed into the POM lattice, forming what Misono has coined the "pseudo-liquid" phase [58]. This characteristic provides an opportunity for reactions to occur not only on the surface of the solid POM cat-

Table 3
Lattice constants of arrays of Wells–Dawson POM salts with the B-$[P_2W_{15}Nb_3O_{62}]^{9-}$ framework

POM	Periodicity of array (Å × Å)	Included angle (°)	Unit cell area (Å^2)
$Na_9[P_2W_{15}Nb_3O_{62}]$	16.3 × 17.8	84.3	288.7
$Cs_9[P_2W_{15}Nb_3O_{62}]$	17.1 × 21.9	59.1	321.3
$(Bu_4N)_9[P_2W_{15}Nb_3O_{62}]$	18.0 × 27.7	63.0	444.3
$(Bu_4N)_5Na_3(Re(CO)_3)[P_2W_{15}Nb_3O_{62}]$	24.5 × 32.9	87.7	805.4

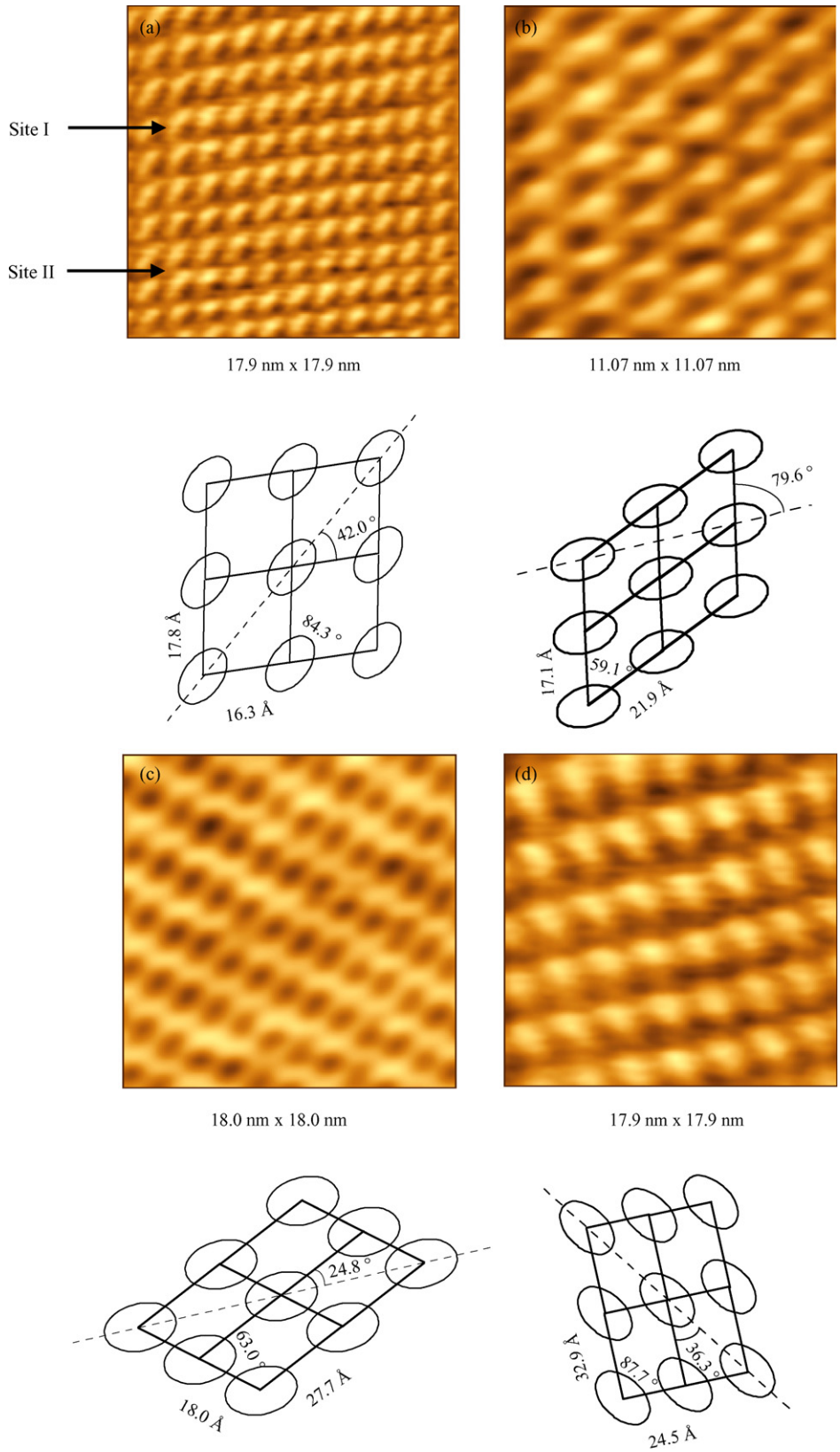

Fig. 6. STM images and unit cells of (a) $Na_9[P_2W_{15}Nb_3O_{62}]$, (b) $Cs_9[P_2W_{15}Nb_3O_{62}]$, (c) $(Bu_4N)_9[P_2W_{15}Nb_3O_{62}]$, and (d) $(Bu_4N)_5Na_3(Re(CO)_3)[P_2W_{15}Nb_3O_{62}]$ arrays on HOPG.

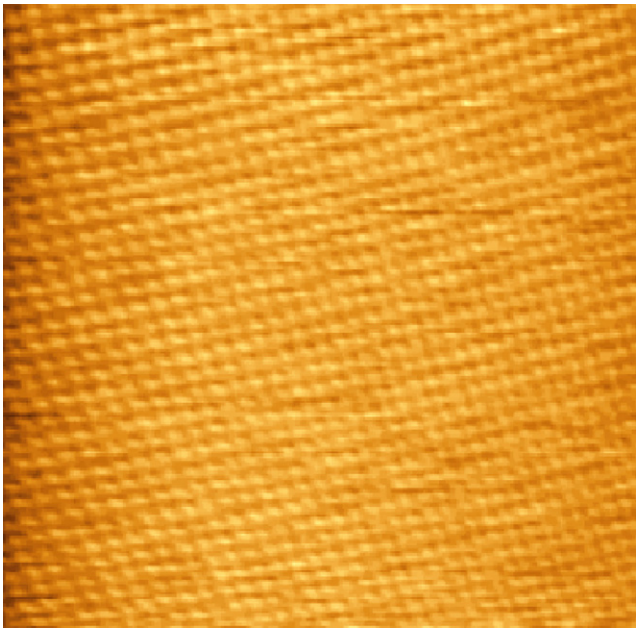

Fig. 7. Large scan-area image of $(Bu_4N)_5Na_3(Re(CO)_3)[P_2W_{15}Nb_3O_{62}]$ array on HOPG. Image area = 90 nm × 90 nm.

alyst, but also in the bulk. In the two-dimensional structures formed on graphite, the array of $H_3PMo_{12}O_{40}$ had a periodicity of 10.8 Å which is roughly the dimension of the spherical Keggin anion, and the protons presumably occupied bridging positions between the anions [23]. Upon ion exchange and subsequent deposition of the ion-exchanged POM salt on graphite, the lattice expanded. The increases in the periodicities reflected the different sizes of the counterions used. In accordance with the secondary structure of Misono [58], the STM studies of $H_3PMo_{12}O_{40}$ and its salts showed that the cations in the ion-exchanged POMs occupied similar bridging positions between the polyanions, thereby increasing the interstitial space between the anions [23]. These observations are not exclusive to members of the Keggin structural class, but they have also been reported for Finke–Droege and Pope–Jeannin–Preyssler two-dimensional structures [27]. Though the cations were not seen in the STM images of Finke–Droege and Pope–Jeannin–Preyssler POM salts, their positions were established from tunneling spectroscopy measurements [24,27]. A typical *I–V* spectrum taken at an interstitial position (Site I) in the array of $Na_9[P_2W_{15}Nb_3O_{62}]$ in Fig. 6(a), and compared to the spectrum of bare graphite is shown in Fig. 8. *I–V* spectra taken at interstitial regions between two polyanions (Site I in Fig. 6(a)) in the STM image all show a broad current plateau (band gap behavior) centered about zero bias and no NDR features. These characteristics are consistent with tunneling spectra taken at regions occupied by cations, as inferred from comparisons with bulk crystalline structures [27]. On the other hand, the *I–V* spectrum taken at the hollow site surrounded by four polyanions (Site II in Fig. 6(a)) exhibited the same *I–V* response as bare graphite, indicating that the array shown in Fig. 6(a) is a monolayer, as previously demonstrated for Keggin-type POM arrays [24–38].

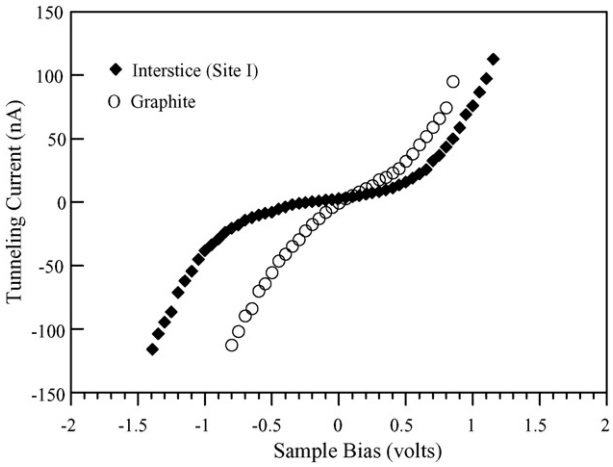

Fig. 8. Tunneling spectrum taken at an Site I in the array of $Na_9[P_2W_{15}Nb_3O_{62}]$ (see Fig. 6(a)), compared to the tunneling spectrum of graphite.

A typical and most reproducible *I–V* spectrum taken atop the corrugations in the STM image of $Na_9[P_2W_{15}Nb_3O_{62}]$ in Fig. 6(a) showed the distinctive NDR behavior at −1.10 V as shown in Fig. 9(a)—evidence that the corrugations imaged were indeed polyanions. Fig. 9(b) shows the distribution of NDR peak voltages of $Na_9[P_2W_{15}Nb_3O_{62}]$ arrays, exhibiting a monomodal distribution with a statistical mean value of -1.04 ± 0.14 V.

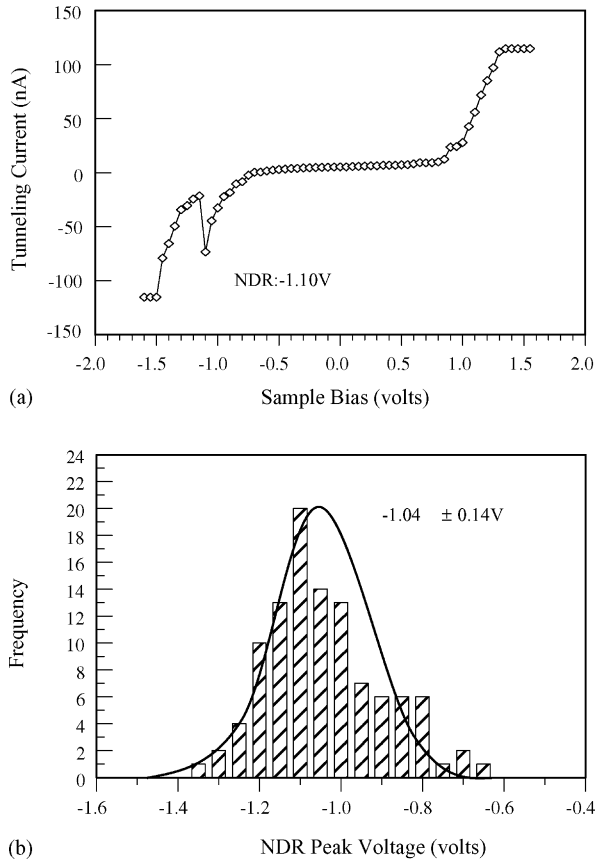

Fig. 9. (a) A typical *I–V* spectrum taken at $Na_9[P_2W_{15}Nb_3O_{62}]$ corrugations (bright features) in Fig. 6(a) showing NDR behavior at −1.10 V. (b) Distribution of NDR peak voltages of $Na_9[P_2W_{15}Nb_3O_{62}]$ arrays with a statistical mean value of -1.04 ± 0.14 V.

Table 4
Most reproducible NDR peak voltages and statistical mean values measured for Wells–Dawson POM salts with the B-$[P_2W_{15}Nb_3O_{62}]^{9-}$ framework

POM	Most reproducible NDR peak voltage (statistical mean value) (V)
$Na_9[P_2W_{15}Nb_3O_{62}]$	−1.10 (−1.04 ± 0.14)
$Cs_9[P_2W_{15}Nb_3O_{62}]$	−1.15 (−1.11 ± 0.16)
$(Bu_4N)_9[P_2W_{15}Nb_3O_{62}]$	−1.20 (−1.15 ± 0.12)
$(Bu_4N)_5Na_3(Re(CO)_3)[P_2W_{15}Nb_3O_{62}]$	−1.05 (−1.02 ± 0.11)

The peak in the fitted distribution at −1.04 V can be taken as the representative NDR peak voltage for this POM catalyst. The most reproducible NDR peak voltages and statistical mean values measured for Wells–Dawson POM salts with the B-$[P_2W_{15}Nb_3O_{62}]^{9-}$ framework are listed in Table 4.

Clearly, if we ascribe the corrugations in Figs. 2 and 6 to the polyanions, we must concede that STM failed to resolve the cations, even the much bulkier tetrabutylammonium groups and metal carbonyls as in $(Bu_4N)_5Na_3(Re(CO)_3)$. However, such observations are not uncommon in STM. A STM image represents contours of local density of states (LDOS) at the Fermi level, E_F [59]. For a metal surface, this would resemble not only contours of the total electron density, but the topography of the surface as well. For adsorbates on metal surfaces, the STM image becomes much more complex, since the electronic interaction between these adsorbates and the metal may exhibit much more pronounced spatial and electronic structure than the clean metal surface [60]. This interaction may lead to modifications in the LDOS such that the electronic states derived from the adsorbate orbitals and probed by STM may deviate significantly from changes in the total DOS induced by the different adsorbed species on the metal surface. Hence, STM contours of the LDOS of the adsorbate-covered surface may not truly reflect its topography or the positions of the ion cores of the adsorbates, and the corrugations in the image may include electronic contributions from some or all of the adsorbed species. Graphite is chemically inert; hence, chemical interactions between it and the polyanions and cations are expected to be minimal. Though the relative contributions of the polyanions and cations to the total DOS, and thus to the contrast and corrugation seen in the STM images of the POM samples, are not yet known, we can postulate that these contributions are derived mainly from the more electron-rich polyanion species, based on the STM studies previously presented [21,23–38]. Strong evidence for this assignment is the accuracy of the shapes of the corrugations (imaged by STM) relative to the molecular anisotropies of POMs (determined from XRD) belonging to the Keggin [5], Wells–Dawson [6], Droege–Finke [39], and Pope–Jeannin–Preyssler [40] structural classes [27]. Nonetheless, contributions from cationic species in the STM images may be masked by the closely associated, electron-rich, higher-contrast, and bulkier polyanions; the presence of the counter cations is manifested by variations in the spacings between the polyanions in the surface monolayers [23,24]. STM has consistently resolved the molecular anisotropies of different polyanions both in the pure acids and in the alkali salts [23–38]. When the structure of the pure acid form of the POM was resolved, the lattice constants accurately reflected the structure and dimensions of the polyanion. However, the lattice constants for POM salt monolayers are always greater than their corresponding anion dimensions, in accordance with the expected secondary structure [58] of POMs. Thus one may conclude that the periodicities of the arrays of trisubstituted Wells–Dawson anions reflect both the dimensions of the $[P_2W_{15}Nb_3O_{62}]^{9-}$ anions (seen by STM) and those of the charge-compensating tetrabutylammonium and alkali cations (not seen by STM, but detected from TS experiments).

XRD data are available for only two of the $Q[P_2W_{15}Nb_3O_{62}]$ ($Q = Na_9$, Cs_9, $(Bu_4N)_9$, $(Bu_4N)_5Na_3(Re(CO)_3)$) salt samples, namely, $Na_9[P_2W_{15}Nb_3O_{62}]$ and $(Bu_4N)_6Na_1[Rh(C_5Me_5)\cdot P_2W_{15}Nb_3O_{62}]$ [61]. Thus, it is appropriate to compare the monolayer structure on graphite and particular cleavage planes of the bulk crystal of the sodium salt, since the chemical identity of the other counterions presumably affects the packing of the POMs [27]. The (1 1 1) plane of $Na_9[P_2W_{15}Nb_3O_{62}]\cdot 2CH_3CN\cdot 23H_2O$ at a depth of 0.50 of the unit cell is shown in Fig. 10. Again, the water molecules have been omitted in this figure for clarity. Sodium cations are shown as unattached dark spheres, while acetonitrile solvent species can be seen near four-fold hollow sites and at sites slightly above each anion. The unit cell in this plane has dimensions $U = 22.56$ Å and $V = 17.27$ Å, with an included angle of 80.94°, compared to the corresponding lattice constants of 17.8 Å × 16.3 Å and an included angle of 84.3° for the monolayer. As we had seen earlier in the images of $Na_6[P_2Mo_{18}O_{62}]$, the Wells–Dawson anions in the STM image of $Na_9[P_2W_{15}Nb_3O_{62}]$ are staggered with respect to each other, but again, this staggering appears to be much more pronounced in the monolayer than in the bulk. It is also apparent that the considerable difference between the magnitude of the *U* vector

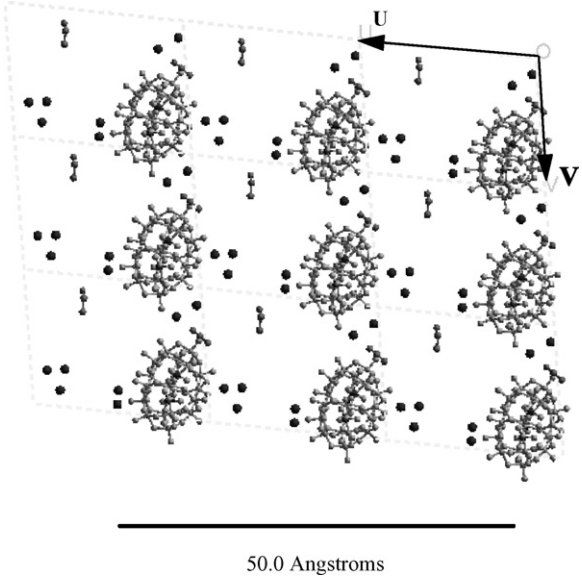

Fig. 10. The (1 1 1) plane of the bulk crystal of $Na_9P_2W_{15}Nb_3O_{62}\cdot 2CH_3CN\cdot 23H_2O$: dark, unattached spheres represent Na^+ cations, and water molecules have been omitted.

(22.56 Å) and the STM-measured value of 17.8 Å is due to the water molecules that dominate the interstitial regions between the polyanions along this direction in the bulk. Along the *V* direction, the agreement between the two values is close (17.27 Å versus 16.3 Å); however, the slight difference may also be due to the solvent species (acetonitrile and water) that position themselves between the anions along this direction in the bulk crystal. Finally, as indicated earlier, the difference in the packing motifs of the polyanions is due to the absence of some of the bulk species (H_2O and possibly CH_3CN) in the POM monolayer, and the absence of intermolecular interactions normal to the surface.

3.3. Correlation between NDR peak voltage and reduction potential

It should be noted that STM images in this work were obtained at positive sample biases with respect to the tip. This means that electrons flow from tip to sample in a normal mode of operation. NDR behavior for POM samples was observed at negative sample biases, i.e., when electrons tunnel from sample to tip. Simple one-dimensional theory predicts that the electron transmission probability between two electronically equivalent electrodes should increase monotonically with increasing applied potential [62]. The NDR phenomenon in tunneling spectra of POMs is recognized as a consequence of a double-barrier resonant tunneling structure or quantum well in which the electron transmission probability decreases with increasing applied potential at a resonance energy level; NDR has been observed consistently for the arrays of Keggin-type POMs [23–38]. A similar explanation for NDR behavior observed for an Anderson-type $[PtMo_6O_{24}]^{4-}$ POM was also reported [63].

We have demonstrated that NDR peak voltages of Keggin-type POMs are closely related to the electronic properties of POMs and, in turn, to the redox properties of Keggin-type POMs [24,26,28–30,32,34–38]. The NDR peak voltages of Keggin-type POM arrays were influenced by the identity of the countercations [24,26,30,36–38], framework transition-metal atoms [26,28–30,34,36–38], heteroatoms [32,35–38], and adsorbed organic molecules [24,29]. Investigation of the Keggin-type POMs revealed that substitution of more electronegative atoms for counter-cations or for the central heteroatom shifted the NDR peaks to less negative voltages, corresponding to increased reduction potentials of the POMs. However, substitution of more electronegative metals into the Keggin framework shifted the NDR peaks to more negative voltages, corresponding to decreased reduction potentials. The most important conclusion was that, regardless of exchange/substitution positions, NDR peaks appeared at less negative potentials for higher reduction potentials of the POMs.

Fig. 11 shows a correlation between NDR peak voltage and reduction potential of Wells–Dawson POM catalysts established for all families of POMs examined in this work. The NDR peak voltages of $[P_2Mo_{18-x}V_xO_{62}]^{(6+x)-}$ ($x = 0, 1, 2, 3$) and $Q[P_2W_{15}Nb_3O_{62}]$ ($Q = Na_9$, Cs_9, $(Bu_4N)_9$, $(Bu_4N)_5Na_3(Re(CO)_3)$) POM samples were taken from Tables 2 and 4, respectively. The reduction potentials of Wells–Dawson POM catalysts were measured by electrochemical method in solution, as described in a previous report [64]. The correlation clearly demonstrates that more reducible Wells–Dawson POM catalysts showed NDR behavior at less negative applied voltages, in the same fashion as observed for Keggin-type POM catalysts [38]. This result implies that NDR peak voltage of Wells–Dawson POMs can be utilized as a single correlating parameter for the reduction potential of the POMs; a less negative NDR peak voltage corresponded to a higher reduction potential of the POM. Thus, NDR peak voltages of supported POMs can provide a selection and design basis for Wells–Dawson POM catalysts efficient for selective oxidation reactions.

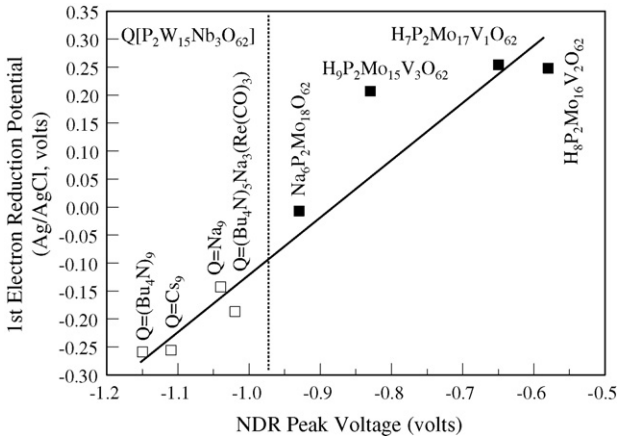

Fig. 11. A correlation between NDR peak voltage and reduction potential of Wells–Dawson POM catalysts established for $[P_2Mo_{18-x}V_xO_{62}]^{(6+x)-}$ ($x = 0, 1, 2, 3$) and $Q[P_2W_{15}Nb_3O_{62}]$ ($Q = Na_9$, Cs_9, $(Bu_4N)_9$, $(Bu_4N)_5Na_3(Re(CO)_3)$). POM samples: open symbol = $Q[P_2W_{15}Nb_3O_{62}]$ series, closed symbol = $[P_2Mo_{18-x}V_xO_{62}]^{(6+x)-}$ series.

4. Conclusions

STM images of Wells–Dawson-type POMs and their salts showed well-ordered two-dimensional arrays of the polyanions on graphite surfaces. The measured periodicities of the POM arrays were consistent with the dimensions and structure of the Wells–Dawson anion. The monolayers of Wells–Dawson salts showed increases in the array periodicities; these increases corresponded to the sizes of the different charge-compensating counter cations. Tunneling spectroscopy experiments suggested that the countercations are roughly uniformly distributed around the polyanions in the monolayers, consistent with their location in the bulk crystal structures. Also, there were pronounced differences between the packing of the polyanions in the bulk and two-dimensional array structures. These differences were explained in terms of the absence of significant numbers of water molecules in the monolayers, and the absence of intermolecular interactions in the direction normal to the plane of the monolayer. The Wells–Dawson POM samples examined in this work exhibited NDR behavior in their tunneling spectra. More reducible POMs showed NDR behavior at less negative applied voltages. The NDR peak voltages of Wells–Dawson POM arrays may therefore serve as a correlating parameter for the reduction potentials of these POM catalysts.

Acknowledgements

Synthesis and characterization of the polyoxoanion samples at Colorado State University were supported by NSF grant CHE-0078436 to R.G. Finke.

References

[1] M.T. Pope, A. Müller, Polyoxometalates: From Platonic Solids to Anti-retroviral Activity, Kluwer Academic Publishers, Dordrecht, The Netherlands, 1994.
[2] I.V. Kozhevnikov, Catal. Rev.-Sci. Eng. 37 (1995) 311.
[3] C.L. Hill, C.M. Prosser-McCartha, Coord. Chem. Rev. 143 (1995) 407.
[4] T. Okuhara, N. Mizuno, M. Misono, Adv. Catal. 41 (1996) 113.
[5] J.F. Keggin, Nature 131 (1933) 908.
[6] B. Dawson, Acta Crystallogr. 6 (1953) 113.
[7] G.M. Maksimov, I.V. Kozhevnikov, React. Kinet. Catal. Lett. 39 (1989) 317.
[8] S. Shikata, S. Nakata, T. Okuhara, M. Misono, J. Catal. 166 (1997) 236.
[9] M. Hölscher, U. Englert, B. Zibrowius, W.F. Hölderich, Angew. Chem. Int. Ed. 33 (1994) 2491.
[10] S.K. Yun, R.J. Pinnavaia, Inorg. Chem. 35 (1996) 6853.
[11] D.K. Lyon, W.K. Miller, T. Novet, P.J. Domaille, E. Evitt, D.C. Johnson, R.G. Finke, J. Am. Chem. Soc. 113 (1991) 7209.
[12] D. Mansuy, J.F. Bartoli, P. Battioni, D.K. Lyon, R.G. Finke, J. Am. Chem. Soc. 113 (1991) 7222.
[13] S. Dong, M. Liu, J. Electroanal. Chem. 371 (1994) 95.
[14] D.J. Edlund, R.J. Saxton, D.K. Lyon, R.G. Finke, Organometallics 7 (1988) 1692.
[15] M. Pohl, D.K. Lyon, N. Mizuno, K. Nomiya, R.G. Finke, Inorg. Chem. 34 (1995) 1413.
[16] H. Weiner, J.D. Aiken III, R.G. Finke, Inorg. Chem. 35 (1996) 7905.
[17] T. Nagata, M. Pohl, H. Weiner, R.G. Finke, Inorg. Chem. 36 (1997) 1366.
[18] R.G. Finke, in: A. Müller, M.T. Pope (Eds.), Polyoxometalates: Self-assembled Beautiful Structures, Adaptable Properties, Industrial Applications, Kluwer Academic Publishers, Dordrecht, The Netherlands, 2001.
[19] B. Këita, L. Nadjo, Surf. Sci. 254 (1991) L443.
[20] B. Këita, F. Chauveau, F. Théobald, D. Bélanger, L. Nadjo, Surf. Sci. 264 (1992) 271.
[21] B.A. Watson, M.A. Barteau, L. Haggerty, A.M. Lenhoff, R.S. Weber, Langmuir 8 (1992) 1145.
[22] M. Ge, B. Zhong, W.G. Klemperer, A.A. Gewirth, J. Am. Chem. Soc. 118 (1996) 5812.
[23] I.K. Song, M.S. Kaba, G. Coulston, K. Kourtakis, M.A. Barteau, Chem. Mater. 8 (1996) 2352.
[24] I.K. Song, M.S. Kaba, M.A. Barteau, J. Phys. Chem. 100 (1996) 17528.
[25] M.S. Kaba, I.K. Song, M.A. Barteau, J. Phys. Chem. 100 (1996) 19577.
[26] M.S. Kaba, I.K. Song, M.A. Barteau, J. Vac. Sci. Technol. A 15 (1997) 1299.
[27] M.S. Kaba, I.K. Song, D.C. Duncan, C.L. Hill, M.A. Barteau, Inorg. Chem. 37 (1998) 398.
[28] I.K. Song, M.S. Kaba, M.A. Barteau, W.Y. Lee, Catal. Today 44 (1998) 285.
[29] M.S. Kaba, M.A. Barteau, W.Y. Lee, I.K. Song, Appl. Catal. A 194 (2000) 129.
[30] M. Kinne, M.A. Barteau, Surf. Sci. 447 (2000) 105.
[31] M.S. Kaba, I.K. Song, M.A. Barteau, J. Phys. Chem. B 106 (2002) 2337.
[32] I.K. Song, R.B. Shnitser, J.J. Cowan, C.L. Hill, M.A. Barteau, Inorg. Chem. 41 (2002) 1292.
[33] I.K. Song, M.S. Kaba, M.A. Barteau, Langmuir 18 (2002) 2358.
[34] M.S. Kaba, I.K. Song, S.H. Wasfi, M.A. Barteau, J. Electrochem. Soc. 149 (2002) E117.
[35] I.K. Song, M.A. Barteau, J. Mol. Catal. A 182/183 (2002) 185.
[36] M.A. Barteau, J.E. Lyons, I.K. Song, J. Catal. 216 (2003) 236.
[37] I.K. Song, J.E. Lyons, M.A. Barteau, Catal. Today 81 (2003) 137.
[38] I.K. Song, M.A. Barteau, Langmuir 20 (2004) 1850.
[39] R.G. Finke, M.W. Droege, Inorg. Chem. 27 (1983) 1006.
[40] M.H. Alizadeh, S.P. Harmalker, Y. Jeannin, J. Martin-Frère, M.T. Pope, J. Am. Chem. Soc. 107 (1985) 2662.
[41] R.G. Finke, D.K. Lyon, K. Nomiya, T.J.R. Weakley, Acta Crystallogr. C 46 (1990) 1592.
[42] R.G. Finke, D.K. Lyon, K. Nomiya, S. Sur, N. Mizuno, Inorg. Chem. 29 (1990) 1784.
[43] A. Trovarelli, R.G. Finke, Inorg. Chem. 32 (1993) 6034.
[44] K. Nomiya, M. Kaneko, N.C. Kasuga, R.G. Finke, M. Pohl, Inorg. Chem. 33 (1994) 1469.
[45] K. Nomiya, C. Nozaki, K. Miyazawa, Y. Shimizu, T. Takayama, K. Nomura, Bull. Chem. Soc. Jpn. 70 (1997) 1369.
[46] K. Nomiya, M. Pohl, N. Mizuno, D.K. Lyon, R.G. Finke, Inorg. Synth. 31 (1997) 186.
[47] R. Strandberg, Acta Chem. Scand. A 29 (1975) 350.
[48] M. Kuwabara, D.R. Clarke, D.A. Smith, Appl. Phys. Lett. 56 (1990) 2396.
[49] I.K. Song, J.R. Kitchin, M.A. Barteau, Proc. Natl. Acad. Sci. U.S.A. 99 (2002) 6471.
[50] B. Herzog, W. Bensch, Th. Ilkenhans, R. Schlögl, Catal. Lett. 20 (1993) 203.
[51] R.G. Finke, M.W. Droege, J. Am. Chem. Soc. 106 (1984) 7274.
[52] R.G. Finke, B. Rapko, R.J. Saxton, P.J. Domaille, J. Am. Chem. Soc. 108 (1986) 2947.
[53] R.G. Finke, B. Rapko, P.J. Domaille, Organometallics 5 (1986) 175.
[54] R.G. Finke, K. Nomiya, C.A. Green, M.W. Droege, Inorg. Synth. 29 (1991) 239.
[55] Y. Lin, K. Nomiya, R.G. Finke, Inorg. Chem. 32 (1993) 6040.
[56] K. Nomiya, C. Nozaki, A. Kano, T. Taguchi, K. Ohsawa, J. Organometal. Chem. 533 (1997) 153.
[57] J.D. Aiken III, Y. Lin, R.G. Finke, J. Mol. Catal. A 114 (1996) 29.
[58] M. Misono, Catal. Rev.-Sci. Eng. 29 (1987) 269.
[59] J. Tersoff, D.R. Hamann, Phys. Rev. Lett. 50 (1983) 1998.
[60] J. Wintterlin, R.J. Behm, in: H.-J. Güntherodt, R. Wiesendanger (Eds.), Scanning Tunneling Microscopy I, Springer-Verlag, New York, 1992.
[61] M. Pohl, Y. Lin, T.J.R. Weakley, K. Nomiya, M. Kaneko, H. Weiner, R.G. Finke, Inorg. Chem. 34 (1995) 767.
[62] D.A. Bonnell, Scanning Tunneling Microscopy and Spectroscopy, VCH, New York, 1993.
[63] A.M. Dykhne, S.Y. Vasil'ev, O.A. Petrii, A.G. Rudavets, G.A. Tsirlina, Dokl. Akad. Nauk. 368 (1999) 467.
[64] I.K. Song, M.A. Barteau, J. Mol. Catal. A 212 (2004) 229.